Received: 14 September 2023 | Revised: 18 December 2023 | Accepted: 21 February 2024

DOI: 10.1002/mrm.30078

RESEARCH ARTICLE

Magnetic Resonance in Medicine

Intra-scan RF power amplifier drift correction

Ali Aghaeifar[1] | Dario Bosch[1,2] | Rahel Heule[1,2,3] | Sydney Williams[4] | Philipp Ehses[5] | Franck Mauconduit[6] | Klaus Scheffler[1,2]

[1]High-Field Magnetic Resonance Center, Max Planck Institute for Biological Cybernetics, Tuebingen, Germany

[2]Department of Biomedical Magnetic Resonance, University of Tuebingen, Tuebingen, Germany

[3]Center for MR Research, University Children's Hospital, Zurich, Switzerland

[4]Imaging Centre of Excellence, University of Glasgow, Glasgow, UK

[5]MR Physics, German Center for Neurodegenerative Diseases (DZNE), Bonn, Germany

[6]NeuroSpin, Paris-Saclay University, Gif-sur-yvette, France

Correspondence
Ali Aghaeifar, High-Field Magnetic Resonance Center, Max Planck Institute for Biological Cybernetics, Max-Planck-Ring 11, 72076 Tuebingen, Germany.
Email: ali.aghaeifar@tuebingen.mpg.de

Funding information
ERC Advanced Grant, Grant/Award Number: 834940; Deutsche Forschungsgemeinschaft (DFG), Grant/Award Number: SCHE 658/12

Abstract

Purpose: The drift in radiofrequency (RF) power amplifiers (RFPAs) is assessed and several contributing factors are investigated. Two approaches for prospective correction of drift are proposed and their effectiveness is evaluated.

Methods: RFPA drift assessment encompasses both intra-pulse and inter-pulse drift analyses. Scan protocols with varying flip angle (FA), RF length, and pulse repetition time (TR) are used to gauge the influence of these parameters on drift. Directional couplers (DICOs) monitor the forward waveforms of the RFPA outputs. DICOs data is stored for evaluation, allowing calculation of correction factors to adjust RFPAs' transmit voltage. Two correction methods, predictive and run-time, are employed: predictive correction necessitates a calibration scan, while run-time correction calculates factors during the ongoing scan.

Results: RFPA drift is indeed influenced by the RF duty-cycle, and in the cases examined with a maximum duty-cycle of 66%, the potential drift is approximately 41% or 15%, depending on the specific RFPA revision. Notably, in low transmit voltage scenarios, FA has minimal impact on RFPA drift. The application of predictive and run-time drift correction techniques effectively reduces the average drift from 10.0% to less than 1%, resulting in enhanced MR signal stability.

Conclusion: Utilizing DICO recordings and implementing a feedback mechanism enable the prospective correction of RFPA drift. Having a calibration scan, predictive correction can be utilized with fewer complexity; for enhanced performance, a run-time approach can be employed.

KEYWORDS

bSSFP, directional coupler, drift, RF power amplifier, run-time correction, satTFL

1 | INTRODUCTION

MRI relies on the precise functioning of complex hardware components. While MRI technology has advanced significantly over the years, one challenge that continues to persist is the occurrence of drift (gradual deviation in the performance over time) in the MRI hardware. Drift in MRI hardware can result in reduced image quality and

decreased reproducibility of imaging studies over time, compromising the accuracy and diagnostic value of the images.

The severity and impact of various hardware drift types on the acquisition process are determined by the employed sequence and utilized protocol. For instance, in MR imaging, drift of the B_0 field can result in image shift along the phase-encoding direction in echo-planar imaging[1] or ineffective fat saturation.[2] In MR spectroscopy, correcting for frequency and phase drift is an essential step as spectral broadening and signal-to-noise ratio loss will impact metabolite signals if not accounted for.[3–5]

Another element within MRI known to undergo drift is the radiofrequency (RF) power amplifier (RFPA). This component is tasked with amplifying the RF pulse in the sequence, and its abnormality in performance results in varying excitation profiles and flip angles (FAs).[6] To compensate, feedback routines can be integrated at the hardware level. It is shown that employing current feedback within an on-coil class-D RFPA system enables obtaining RF envelope information in terms of amplitude and bandwidth, thereby achieving load-insensitive operation.[7] Another work demonstrates the potential application of Cartesian feedback to control in-phase and quadrature components of the current delivered to a RF coil.[8] This method was subsequently expanded to integrate a band-pass error amplifier, addressing sensitivity issues related to phase or amplitude discrepancies as well as DC offsets in the feedback loop.[9] However, there are instances where corrections can be delayed or compromised during specific acquisition protocols where RFPA undergo high thermal stress when they are subjected to high duty cycle tasks.

Correction of RF pulse imperfections can be expanded to software level, offering increased reproducibility and flexibility for the development and testing of algorithms. A study shows RF envelope can be adjusted iteratively using basic signal addition and subtraction to achieve a desired excitation profile without requiring compensation for nonlinearities in the RFPA.[10] Another approach involves utilizing a current sensor[11] and supplying the RFPA with predistorted input, aiming to rectify offset, non-linearity, coupling, and temporal errors.[12] The predistortion technique can also be implemented using data gathered from field sensors.[13] In the context of parallel excitation pulses where a rapidly changing envelope is typical, a regularization technique has been proposed to mitigate distortions arising from the memory effect of the RFPA.[14] Despite not being currently utilized, these methods hold potential for compensating RFPA drift with certain modifications. However, they depend on external hardware, iterative processes, or calibration scans for their implementation.

At ultra-high field (UHF) MRI, this issue becomes notably more troublesome as greater power requirements arise, often necessitating RF power up to 10–32 kW.[6,8] Consideration should also be given the requirement of multiple RFPAs needed for RF transmit arrays which are in most cases preferred to volume body coils at UHF in order to mitigate B_1^+ inhomogeneity.[15,16] Multiple RFPAs outputs can be combined and later split or individually utilized to drive a pTx array coil. The output drift may vary between RFPA revisions (model numbers), which can be problematic when malfunctioning units are replaced with newer models with an updated hardware design. Additionally, differences in RF waveforms played out in individual channels, often associated with tailored pTx RF pulses, can also contribute to different drift behaviors as the RFPA transfer function does not necessarily offer a constant power gain factor,[6] and the drifting behavior might also exhibit variations under varying stress conditions.

RFPA drift is a critical aspect to consider to obtain comparable results in inter-site and intra-site reproducibility studies. The impact of RFPA drift on quantitative imaging was recently investigated as part of the traveling head 2.0 multicenter study at 7T.[17] It was observed that the RFPA behavior differed across sites. Despite an average deviation of 6.3% in the measured B_1^+ between the individual UHF sites with different hardware and software versions, comparable results were obtained. However, by employing calibration data to correct for RFPA drift retrospectively, the observed initial differences between the different centers could be reduced by 8.1% for chemical exchange saturation transfer (CEST) relayed nuclear Overhauser effect (rNOE) maps. The repeatability of high-resolution multiparameter mapping was evaluated in a separate multisite study conducted at 7T.[18] All five sites had a scanner equipped with identical hardware and configuration (which was not the case for the traveling head study). While multiparameter mapping measurements generally exhibited a good level of repeatability, consistently across all sites, the magnetization transfer saturation (MTsat) map exhibited the highest coefficient of variation (CV), indicating lower repeatability. Furthermore, using the Bloch–Siegert shift[19] B_1^+ mapping method for transmit inhomogeneity correction, the R_1 and proton density (PD) maps demonstrated slightly higher CV. Given the utilization of RF pulses with extended duty cycles in CEST, Bloch–Siegert shift, and MTsat sequences, we suspect that RFPA drift might be a principal factor underlying the reduced repeatability observed in the MTsat, R_1, and PD maps in Reference 18. This reasoning gains credence from the fact that the scanners utilized in these investigations are outfitted with unregulated amplifiers, which are not specifically tailored for quantitative MRI (qMRI) applications.

In this study, our initial focus is to examine the behavior of RFPA under specific protocols in order to evaluate the influences of various factors and dependencies on RFPA drift, as well as their reproducibility. We provide evidence of RFPA drift based on phantom and in vivo scans and compare the drift-affected data with their corresponding drift-compensated counterparts. We demonstrate the utilization of calibration data for prospective drift correction. Furthermore, we propose a method to monitor the output of RFPA and effectively correct for any potential deviations by providing run-time feedback to the imaging sequence. Lastly, we discuss some strategies aimed at reducing impact of RFPA drift in the reconstructed data.

2 | METHOD

2.1 | MRI measurement setup

All measurements were performed and data were collected on a MAGNETOM 9.4T MRI scanner (Siemens Healthcare) running Syngo VE12U software. The scanner was equipped with an SC72 whole-body gradient coil with a maximum amplitude and slew rate of 70 mT/m and 200 T/m/s, respectively. A 16-channel pTx system was utilized to enable RF transmission, with eight of those channels being newly added following a scanner upgrade. As provided by the scanner manufacturer, the Tx coils were driven by 16 separate RFPAs of which 8 were of a more recent design. In the subsequent sections, the former and updated RFPA designs are denoted as group 1 and group 2, respectively. A custom built head array coil with 16 transmit and 31 receive elements was used for RF transmission and signal reception.[20]

Given the limited availability of the MAGNETOM 9.4T MRI scanner, the evaluation of inter-pulse RFPA drift assessment (as detailed below) was partially repeated on Siemens MAGNETOM 7T Plus, Siemens MAGNETOM 7T Terra, and Siemens ISEULT MAGNETOM 11.7T MR scanners to assess RFPA behavior at other frequencies. The RFPAs for all four scanners are manufactured by Comet (Comet XYLON international GmbH). The MAGNETOM 9.4T and MAGNETOM 7T Plus MR scanners use 1 kW RFPA units, whereas the MAGNETOM 7T Terra and ISEULT MAGNETOM 11.7T MR scanners are fitted with 2 kW RFPA units.

2.2 | RFPA drift assessment

As an internal part of the pTx safety system, each of the RF transmission lines incorporates directional couplers (DICOs), which are responsible for monitoring the forward and reflected waveforms and enabling inline calculation of specific absorption rate (SAR). The measurements obtained from a DICO are digitized using a sampling rate of 1 MHz. By activating a switch through the scanner's command line interface, the digitized data can be saved in its raw form, allowing for later retrieval, analysis and processing. The forward values recorded by DICOs were utilized in this study to evaluate RFPA drifts. The literature has also reported various other applications by utilizing the recorded values from DICOs.[21–23]

2.2.1 | Inter-pulse drift

An RF-only sequence without gradients was employed to investigate impact of RF length, RF FA, and pulse repetition time (TR) on RFPA drift. For simplicity, a nonselective rectangular pulse was used and applied in all measurements until the RFPA output became stable and the drifting ceased. The measurements were repeated by adjusting one parameter within a given range while keeping the other two factors constant. In consideration of hardware safeguards, the highest analyzed RF duty-cycle—defined as the ratio of RF length to TR—was 66.6%. The ranges of FA, TR, and RF length investigated in this study are reported in Table 1.

An assessment of inter-pulse drift between scanners was conducted by configuring the transmit voltage of each RFPA to generate a 10 V rectangular RF pulse. Applying the default scaling factor of $\frac{\sqrt{nTx}}{nTx}$, where nTx represents the number of transmit channels, this equates to setting the system transmit voltage at 40 V for the MAGNETOM 9.4T, which has 16 transmit channels, and at 28.284 V for other scanners equipped with eight transmit channels. Measurements were iterated across TR intervals ranging from 3 to 21 ms, with increments of 3 ms. RF duration fixed at 1.5 ms remained constant throughout the experiment.

2.2.2 | Intra-pulse drift

A sequence using only RF pulses, resembling inter-pulse assessment, was utilized. The duration of each RF pulse was set at 15 ms and executed 50 times. TR was extended to 10 s to ensure sufficient relaxation of the RFPAs before the commencement of the subsequent RF pulse. The determination of this 10-s TR duration was based on experimental evaluation and could vary for different RFPA models. The study was replicated using various RFPA transmit voltages spanning from 12.5 to 175 V (Table 1), with the highest allowable transmit voltage per channel being 200 V.

TABLE 1 Flip angle (FA), pulse repetition time (TR), radiofrequency (RF) length, and transmit voltages examined for inter-pulse and intra-pulse RF power amplifiers (RFPA) drift assessment.

	FA (deg.)	TR (ms)	RF length (ms)	Transmit voltage[a] (V)
Inter-pulse	10	3:3:21[b]	0.2, 0.4, 0.8, 1.2, 2	15.5, 9.3, 4.5, 3, 1.8
	10	6:3:24	4	0.9
	10	9:3:27	6	0.475
	10	12:3:30	8	0.47
	30	3:3:21	1.2	9.3
	60	3:3:21	1.2	18.2
Intra-pulse	—	10 000	15	12.5, 25, 50, 75, 100, 125, 150, 175

[a] This represents the transmit voltage on the RFPA output after accounting for the system scaling factor of 0.25 for 16 transmit channels.
[b] MATLAB notation: initial value:increment:last value.

2.3 | Drift correction

2.3.1 | Predictive correction

Two scans were conducted, and the DICOs samples recorded during the first scan were utilized to correct for the drift in the second run. The transmit voltage of each RF pulses was scaled to achieve a similar excitation FA as the previous pulse. Correction factors were calculated as:

$$\mathrm{CF}_{n,c} = \frac{\sum_{m=1}^{L} |\mathrm{RF}_{n,c}[m]|}{\sum_{m=1}^{L} |\mathrm{RF}_{n-1,c}[m]|}, \quad n \in [2, N], c \in [1, 16], \quad (1)$$

where the correction factor $\mathrm{CF}_{n,c}$ was calculated for the nth RF pulse with L samples and cth Tx channel and with N RF pulses in total played out in the sequence. The correction factors were saved in a text file and subsequently loaded before the second sequence started. The corrections table had dimensions of $N \times 16$, where 16 represents the number of Tx channels, and N represents the number of executed RF pulses. During run-time, the transmit voltage of each individual Tx channel was updated for each TR.

2.3.2 | Run-time correction

The reconstruction pipeline was modified to incorporate the reading and sorting of DICOs output in parallel with data acquisition. This modification enabled the pipeline to provide real-time feedback to the ongoing sequence. The modification was implemented using the vendor's reconstruction software called image calculation environment (ICE). Unlike the predictive approach, where the nth RF pulse was used to calculate the scaling for $(n+1)$th RF pulse, a constant RF pulse in the sequence was used as a reference. This means that in Equation (1), the chosen RF in the denominator remained fixed (typically, the first RF can function as an appropriate reference). The correction factor obtained from the nth RF was then applied to correct for the $(n+m)$th RF, where m is an integer greater than or equal to 1 and its value is determined by factors such as the duration of the RF, TR, and the time necessary for inline calculations.

2.4 | Imaging protocols

The evaluation of RFPA drift correction was conducted using a balanced steady state free precession (bSSFP) sequence and B_1^+ mapping using a two-dimensional presaturation TurboFLASH (satTFL)[24] sequence. A polymer-based phantom with short T_1 (≈460 ms) was utilized to attain steady-state faster and mitigate the overlap between RFPA drift and transient states in bSSFP. For bSSFP measurments, a single 3-mm slice was measured with 40 repetitions. The images were acquired using sign-alternated RF pulses, preceded by 100 dummy RF pulses to ensure a steady-state condition. The acquisition protocol included field of view: 192 × 192 mm^2, resolution: 1.5 × 1.5 mm^2, TE/TR: 1.6/3.2 ms, FA: 15°, and RF duration of 1 ms (sinc pulse with time-bandwidth product of 2.0). The first RF pulse (played out as a dummy scan) was chosen as reference for run-time correction. Phase-encoding lines were acquired with both a linear and a centric reordering scheme. The pairing strategy was used for eddy current compensation in centric reordering.[25] The satTFL measurement comprised five unsaturated scans repeated consecutively, followed by one scan prepared using a presaturation pulse. To minimize the impact of T_1 on the measured B_1^+, a centric reordering scheme was employed during the readout. Similar to the bSSFP scans, the initial RF pulse was selected as the reference. The acquisition protocol included field of view: 220×220 mm^2, resolution: 3.4×3.4 mm^2, TE/TR: 1.57/4920 ms, FA: 5°,

and RF duration of 1 ms. Two healthy volunteers for bSSFP measurements and one healthy volunteer for satTFL measurements underwent scanning in compliance with the policies and procedures of the local research ethics guidelines. Field of view increased to $222 \times 222\,mm^2$ for bSSFP in in vivo scans, and only the linear reordering scheme was applied and assessed.

3 | RESULTS

Figure 1 illustrates the drift of 16 RFPAs across 10 000 pulses, with RF Length = 1.2 ms, TR = 3 ms, and FA = 10°. Each data point on the graph corresponds to a single RF pulse. The integral of RF magnitude is computed, and the percentage change relative to the initial RF is depicted to visualize the magnitude drift. In this scenario, the highest drift is observed in the case of Tx 16, reaching a value of 23.3%. The plot reveals the distinction between two distinct groups of RFPA behavior, with one exhibiting less drift than the other. Additionally, the graph indicates that a subset of RFPAs displays fluctuations deviating from the overall trend. Phase drift is determined by calculating the average phase value from the central portion of the RF waveform, which is then subtracted from the phase of the initial RF.

Figure 2 displays a synopsis of the inter-pulse RFPA drift evaluation across a range of RF lengths and TR values. Two heatmaps are employed to distinguish the performance of distinct RFPA groups. In this depiction, the color and numerical value denote the average of the maximum drift and the highest drift observed among all RFPAs within the respective group, respectively. It is evident from Figure 2 that there is a correlation between maximum drift and RF duty-cycle. A lengthier RF pulse combined with a shorter TR results in an increased drift within RFPAs. When the ratio of RF length to TR remains constant, the maximum drift consistently falls within a similar range.

Figure 3 displays RFPA drift results for different flip angles. The results indicate that when maintaining a constant RF length and repetition time (fixed RF duty-cycle), the impact of the FA on the maximum drift is marginal (corresponding transmit voltages are listed in Table 1). This measurement was conducted using an RF length of 1.2 ms.

Figure 4 illustrates the plots displaying the drifting of RFPAs obtained from the inter-scanner assessment conducted with an RF length of 1.5 ms and TR ranging from 3 to 21 ms. The average drift values in percentage for RFPAs at TR = (3, 21 ms) for the involved scanners are as follows: 9.4T group1 and group 2 (25.6%, 2.6%) and (11.0%, 1.4%), 7T Plus (7.9%, 1.2%), 7T Terra (10.9%, 1.2%), and 11.7T (15.7%, 2.3%). Notably, it is observed that the drift

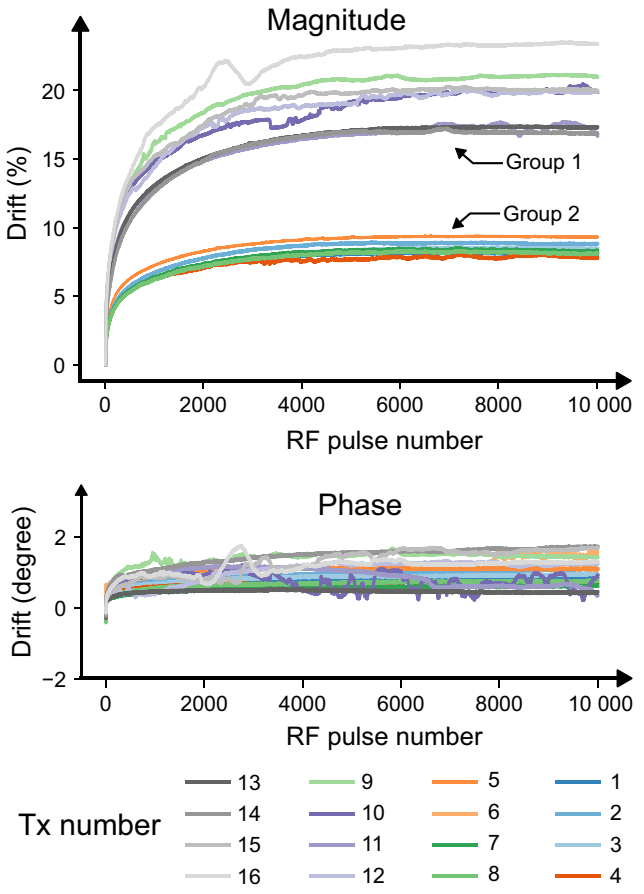

FIGURE 1 Drift of the output of radiofrequency (RF) power amplifiers (RFPAs) during the execution of 10 000 RF pulses with FA of 10° and a duration of 1.2 ms. Pulse repetition time (TR) was set at 3 ms. Transmit channels 1–8 belong to group 2, exhibiting minor drift, while the remaining transmit channels belong to group 1 following the earlier RFPA design. Channels 4 and 16 exhibit the least and greatest magnitude drift, at 7.7% and 23.3%, respectively. To quantify magnitude drift, the integral over the magnitude of samples from directional couplers (DICOs) records is computed for each pulse, then relative change with respect to the first RF pulse is calculated. Phase drift is determined by calculating the difference between the average phase values extracted from the central portion of DICOs samples in the current RF pulse and initial RF pulse.

pattern reverses and begins to decrease after reaching its peak at 7T Terra and 11.7T.

Figure 5 depicts the intra-pulse drift across a range of transmit voltages, averaged over 50 RF pulses each with a duration of 15 ms. After removing the initial and final 200 samples (equivalent to 200 us) to eliminate overshoots and undershoots, the magnitude and phase values are normalized to and subtracted from the initial sample, respectively. The plot highlights contrasting RFPA behaviors between low and high transmit voltages. In the case of low transmit voltage, the magnitude drift indicates an increase in RFPA output voltage, while the phase drift remains negligible. Nevertheless, when the transmit voltage exceeds 100 V per

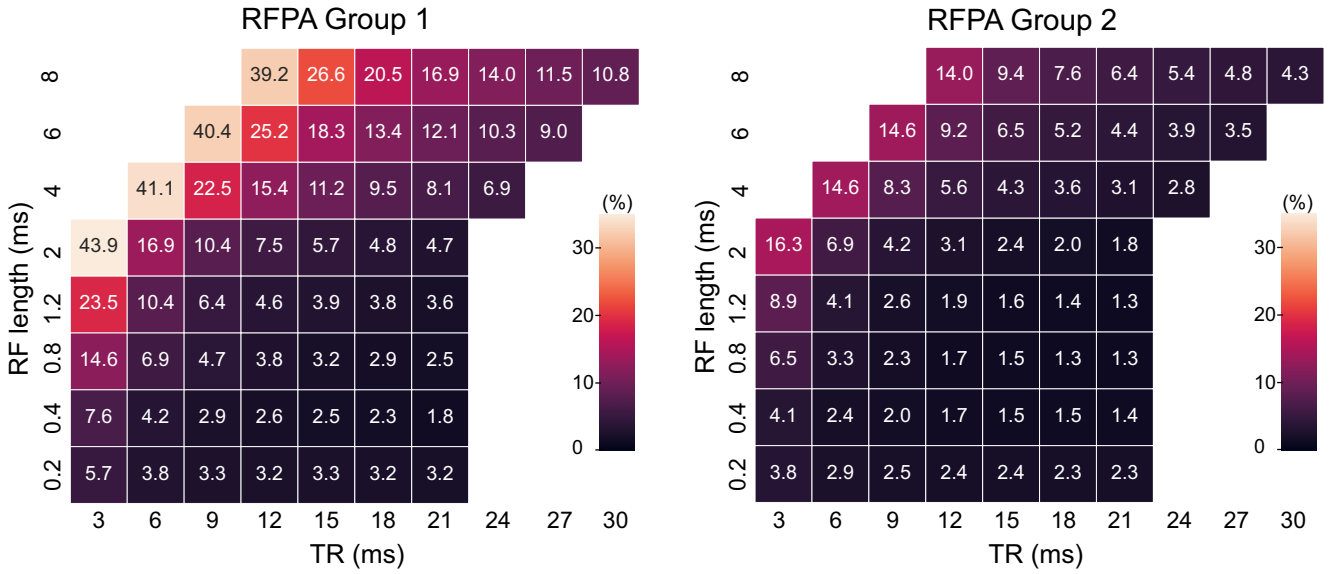

FIGURE 2 The inter-pulse drift percentages are presented for various radiofrequency (RF) lengths and pulse repetition time (TR). The color and number indicate the average and maximum drift, respectively, for the radiofrequency (RF) power amplifiers (RFPAs) in each group. Each group comprises eight RFPAs. Notably, RFPAs in group 2 exhibit reduced drift, especially under high RF duty-cycles. The highest RF duty-cycle considered in the examination is 66.6%. Each block in the heatmap has its own drift plot, as representatively depicted in Figure 1.

RFPA channel, the RFPA exhibits negative drift, leading to a decline in output voltage, a phenomenon commonly referred to as voltage droop. Furthermore, the phase drift demonstrates more pronounced changes, particularly at very high transmit voltages. Output of transmit channel 1 is depicted in Figure 5. Similar behavior is observed in the other transmit channels as well, with the exception that the threshold voltage at which drift direction changes and voltage droop becomes evident is variable and ranges from 100 to 125 V.

Figure 6 illustrates the outcomes of bSSFP imaging under three scenarios: without correction, with predictive correction, and with run-time correction, all observed with an ascending k-space acquisition order. For comparison, the bSSFP acquisition was repeated with a centric k-space order. The uncorrected results from this experiment are shown in the last row of Figure 6 (fully corrected results are presented in Figure S1). In the initial column, unprocessed images from the 40th repetition, where steady-state is attained, are displayed. It is noticeable that image intensity is marginally greater when no correction is applied, aligning with simulations indicating that a slight increase in steady-state signal occurs when the target flip angle (FA) of 15° is raised by a small percentage (Figure S2). The images contain the signal intensity values for three arbitrarily selected voxels.

The second, third, and fourth columns within Figure 6 present CV for the initial 10, last 10, and complete repetitions, respectively. CV is computed voxel by voxel within each scan of bSSFP along the repetition dimension. This approach is used to highlight temporal behavior of RFPA drift which manifests itself along the repetition dimension. The first repetition is omitted to reduce signal deviations arising from the transient state. The inclusion of RFPA drift corrections in the measurements results in greater temporal consistency which is reflected by lower CV values. It is demonstrated that, in contrast to the scenario without any correction, CV maps exhibit similarity across a range of continuous repetitions in both predictive and run-time drift correction methodologies. The outcomes obtained from centric ordering without correction also indicate higher CV compared to its corresponding linear ordering.

The last column in Figure 6 displays the evolution of voxel intensity across all repetitions for the point marked with a blue cross in the first column. It is observed that voxel intensity increases in presence of RFPA drift for the protocol utilized in this study. In this particular measurement, the RFPAs experience a drift of 10.0% ± 4.1% (mean ± SD) in relation to the initial dummy pulse. However, this drift is reduced to 0.64% ± 0.46% and 0.003% ± 0.027% through the implementation of predictive and run-time correction, respectively.

Figure 7 illustrates the in vivo outcomes of RFPA drift correction. Due to the extended T_1 relaxation times of white matter and gray matter at 9.4T,[26] a lengthier preparation phase is necessary for bSSFP to achieve a steady state. Given that a set of 100 dummy scans are employed in the measurements, data from the initial seven repetitions are omitted in CV calculations to mitigate the impact of the

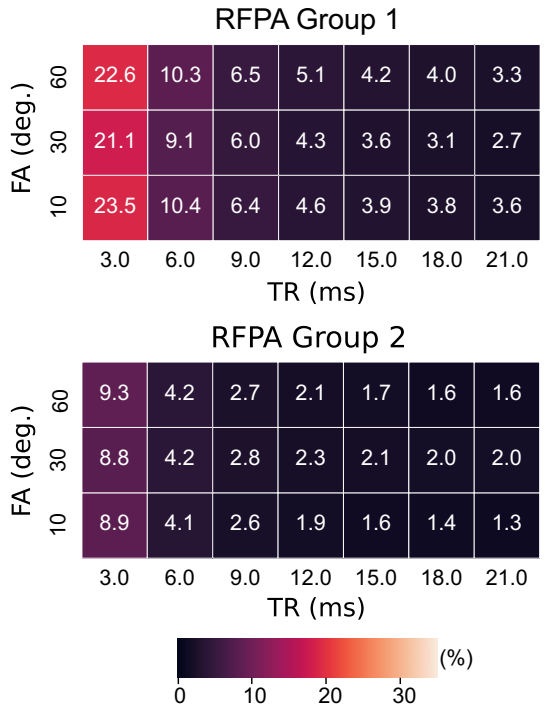

FIGURE 3 The dependence of maximum and average drift on flip angle (FA) is assessed across a range of FA and pulse repetition time (TR), using an RF pulse duration of 1.2 ms. Within this investigated low transmit voltage range, the impact of FA on drift is found to be negligible.

transient state. Columns 1, 2, and 3 display the CV values for the first 10, last 10, and entire set of repetitions, respectively. The last column shows the evolution of average signal intensity within the ROI depicted by blue and green circles over 40 repetitions in the unprocessed image. The prolonged transient phase is evident in the plots. There is a slight disparity in image intensity between the uncorrected and RFPA drift-corrected results. This finding aligns with the simulation outcome depicted in Figure S2. The average signal intensity in both ROIs during the last 10 repetitions is 3.4% higher when drift correction is disabled compared to the scan utilizing run-time correction. The results of similar analysis for the second subject are depicted in Figure S3.

Figure 8 depicts the drift observed in RFPAs over the scan shown in Figure 7. For clarity, only the drift of four RFPAs is displayed, two from group 1 and two from group 2. Each point on the plot represents the integral over the magnitude of one RF pulse. Averaging over 16 RFPAs, the drift is approximately $10.1\% \pm 4.1\%$, which is subsequently mitigated to $0.61\% \pm 0.44\%$ and $-0.002\% \pm 0.014\%$ through the utilization of predictive and run-time correction methods, respectively. Notably, one channel exhibits some deviation from its linear trend in predictive correction approach.

Figure 9 illustrates the comparison of B_1^+ obtained using the satTFL sequence with RFPA drift correction in both off and on states. First, five sets of B_1^+ maps are generated from the combination of five consecutive repetition of unsaturated scans along with a presaturated scan. Then, the relative difference between the fifth and fourth B_1^+ maps and between the fifth and the first B_1^+ maps is computed for both sets of measurements. It is observed that with drift correction off and on, the relative difference between the fifth and fourth B_1^+ is minimal because RFPAs are in a steady condition. However, the relative difference between the fifth and the first B_1^+ is higher when drift correction is off. Conversely, when drift correction is activated, this difference remains minimal again. Within the given slice, approximately 21.4% and 4.1% of voxels exhibit a difference larger than 3% in their B_1^+ value for the cases of drift correction off and drift correction on, respectively.

4 | DISCUSSION

In this study, we conducted an evaluation of RFPA drift and examined several contributing factors. With the aim of real-time measurements of forward/reflected signal through DICOs, the extent of drift can be quantified during any scanning. Here, we utilized DICO feedbacks and introduced two approaches for prospective corrections of RFPA drift. Utilizing RF current and voltage sensors,[11] pick-up coils,[27,28] gradient reversal approach to evaluate RF (GRATER),[29] and magnetic field monitoring using NMR sensors[30] are alternative methods proposed in the literature for RF monitoring and potentially for measuring RFPA drift. When compared to DICOs, pick-up coils may offer certain advantages, such as providing additional information that might not be necessary for drift correction and offering a more direct approach. However, incorporating pick-up coils requires modifications for each RF coil, whereas DICOs are already integrated into the transmission pipeline, making them a more convenient choice.

A typical initial drift curve for a train of short RFs appears to align with a two-term power series model expressed as $ax^b + c$. Here, the variables a, b, and c represent variable coefficients, while x denotes the drifting samples. However, it is understood from the assessment study that the drift evolution varies from one protocol to another. Furthermore, in instances where hardware designs are not fully matched, as in this work, the drift behavior of RFPAs can exhibit discrepancies. Hence, in addition to the two presented methods for drift correction, the utilization of an empirical model incorporating relevant protocol parameters could potentially offer a prediction of drift, even though this aspect was not explored in this study.

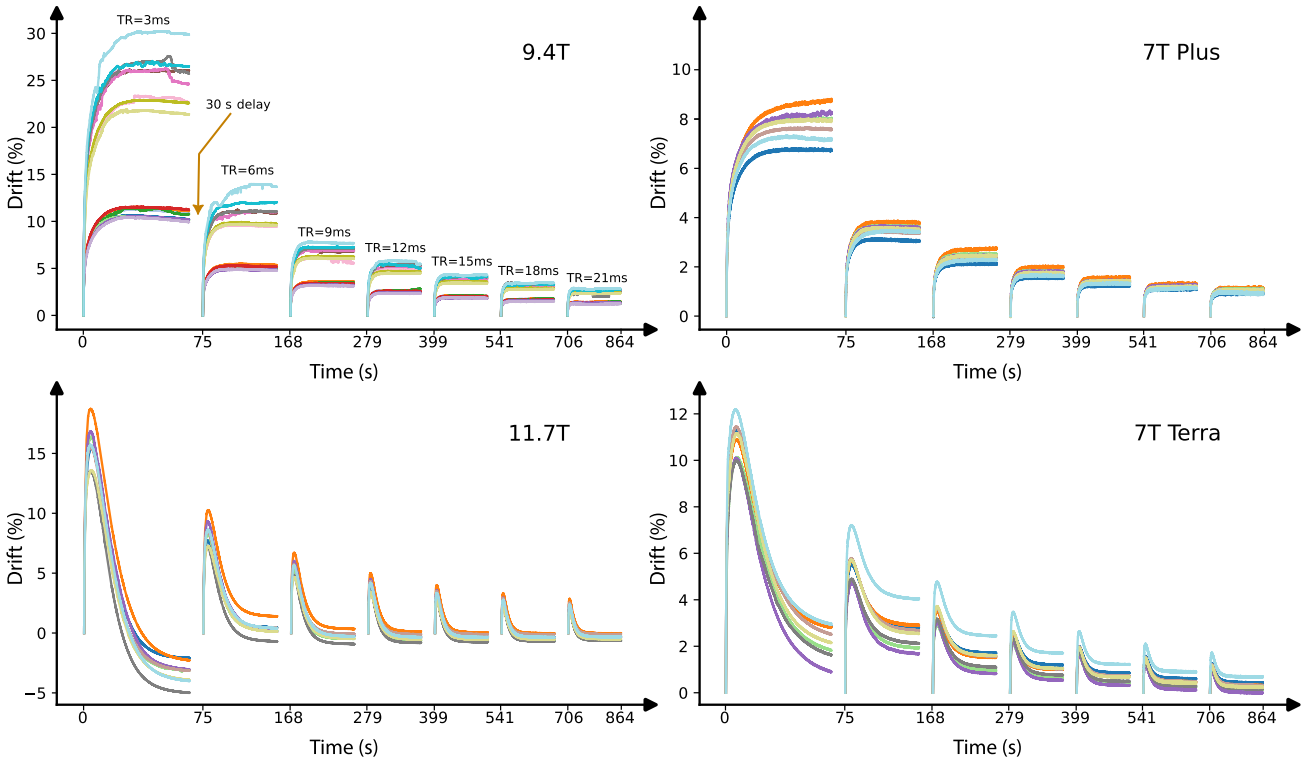

FIGURE 4 The evaluation of intra-pulse drift across four scanners from the same vendor at three distinct field strengths and equipped with radiofrequency (RF) power amplifiers (RFPAs) from the same manufacturer. A rectangular RF pulse of 10 V lasting 1.5 ms was played out at certain pulse repetition time (TR). Measurement was repeated at TRs ranging from 3 to 21 ms. A 30-s interval was introduced between each repetition to allow the RFPAs to relax. When moving toward repetitions with smaller RF duty-cycles, the number of RF pulses played out decreased due to the anticipated settling of RFPAs after fewer RF pulses. Please note that one of the Tx channels in the 7T Plus plot has been omitted due to malfunction.

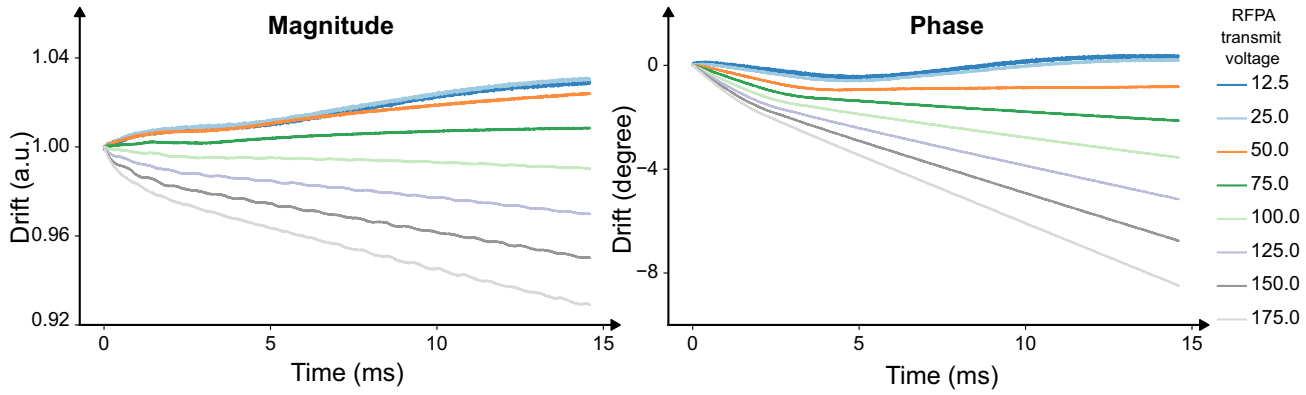

FIGURE 5 The intra-pulse drift of transmit channel 1 was assessed by executing a 15 ms radiofrequency (RF) pulse across a range of transmit voltages. The RF pulse was repeated 50 times and the directional coupler (DICO) samples from these runs were averaged. A 10-s interval between consecutive RF pulses allowed for relaxation of radiofrequency power amplifiers (RFPAs). To process the data, the first and last 200 samples were excluded to eliminate overshoots and undershoots. Subsequently, the magnitude of the samples were normalized to the initial sample and the phase of the samples were subtracted from the initial sample. The plot reveals a tendency for intra-pulse drift to rise at low transmit voltages, which gradually diminishes as the transmit voltage increases, until it begins to decline after reaching 100 V. This loss in output voltage is known as voltage droop. In contrast to low transmit voltages, the phase drift becomes more pronounced at higher transmit voltages.

RFPAs are susceptible to voltage droop regardless of the transmit voltage. This is because of the rise in the temperature of the RF transistors which which often leads to a decrease in gain.[6] However, it is highly plausible that the circuitry of the RFPA employed in this study includes capacitor banks intended to discharge and counteract the

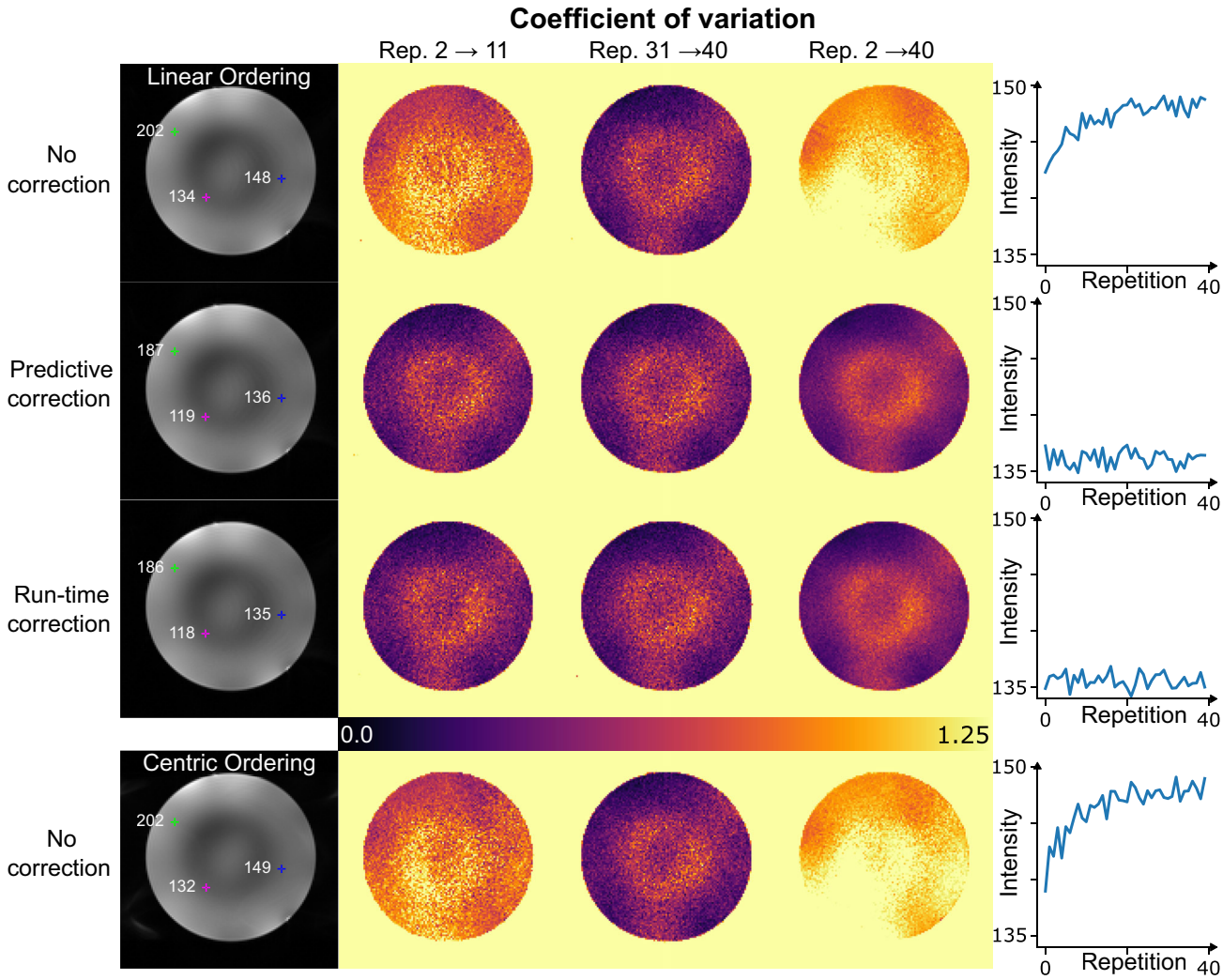

FIGURE 6 A comparison between no radiofrequency (RF) power amplifier (RFPA) drift correction, predictive RFPA drift correction, and run-time RFPA drift correction in a phantom study. The initial repetition is excluded from the analysis to mitigate the impact of the transient state. The first column displays reconstructed images from the 40th repetition. The intensities of three selected voxels are depicted, revealing higher intensity in the absence of correction. Coefficient of variation (CV) is computed across three intervals: the first 10 repetitions, the last 10 repetitions, and all repetitions combined. The application of RFPA correction results in more consistent CV values. The last column showcases the evolution of the voxel marked with a blue cross across all repetitions. Notably, both predictive and run-time corrections yield more stable intensity profiles in comparison to the scan without any correction. The final row presents the same scan with a centric ordering scheme, illustrating the greater sensitivity of centric ordering to RFPA drift.

droop effect. The effectiveness of these capacitors can be dictated by the energy they store and the rate at which they discharge make them optimal for specific operational range, potentially leading to overcompensation or undercompensation in other voltage ranges. Both RF transmit voltage and pulse duration are significant factors. It is expected the droop effect becoming noticeable at lower voltages when the RF pulse duration is getting longer. It is plausible that at lower transmit voltages for a regular short RF pulse, an overcompensation for RFPA output leads to an observable increase in drift, as depicted by the upward trend in Figure 1. The experiments which are not employing a high RF power—which is the case in the imaging protocols of this study and wide range of protocols—were observed to be immune against voltage droop and did not experience a significant phase drift. Consequently, the corrections were exclusively computed based on the magnitude of DICOs records in this work.

The inter-scanner assessment of inter-pulse drift indicates a similar trend between 9.4 and 7T Plus scanners, while 11.7 and 7T Terra exhibit a distinct pattern. At 11.7 and 7T Terra, the drift curve shifts direction, beginning to decrease after reaching to its peak. This results in prolonged drifting and requires more time for RFPAs to settle. This difference might be attributed to the design variation, with 2 kW amplifiers used in 11.7 and 7T Terra

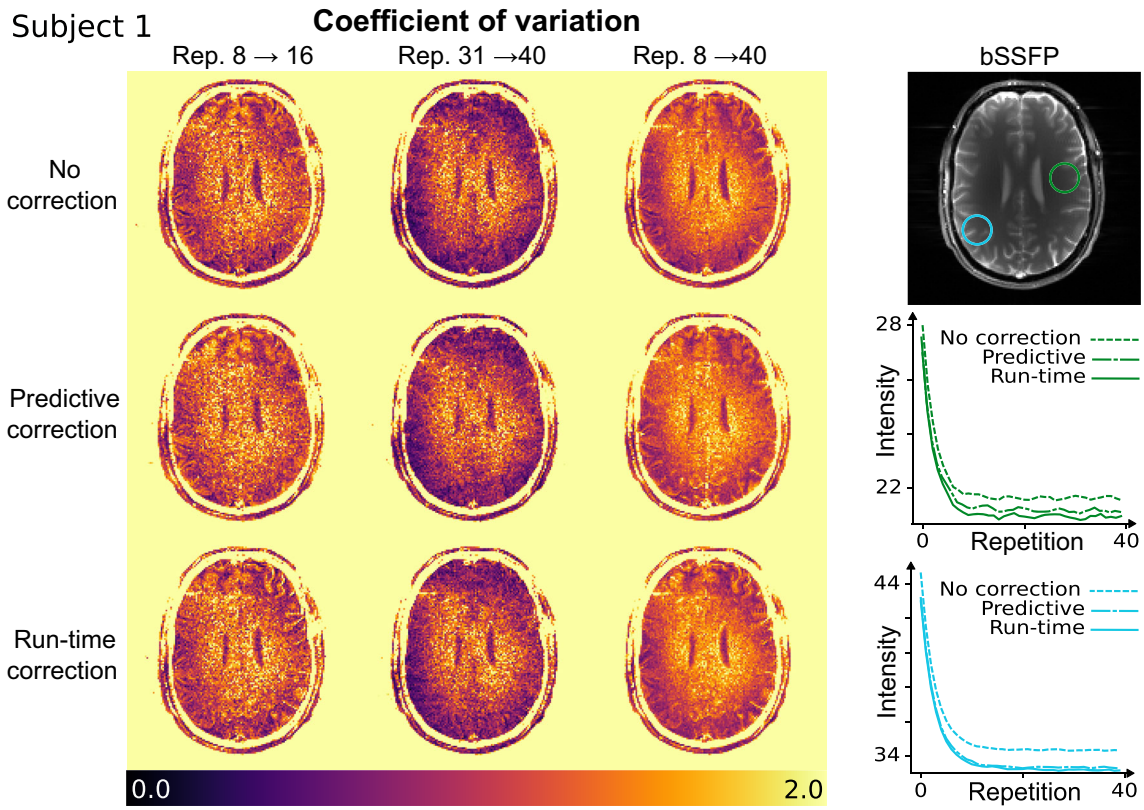

FIGURE 7 A comparison through coefficient of variation (CV) calculation is performed between no radiofrequency (RF) power amplifier (RFPA) drift correction, predictive RFPA drift correction, and run-time RFPA drift correction using data from the first subject. The initial seven repetitions out of 40 repetitions are excluded from the analysis to mitigate the impact of the transient state. However, due to the extended T_1 of gray matter and white matter at 9.4T, CV computed in Columns 1–3 is influenced by a combined contribution from both bSSFP transient state and RFPA drift. The difference in CV between RFPA drift corrected and uncorrected cases across the three intervals is minimal. It is evident that the transient state predominates in the first 10 repetitions for all three cases with and without RFPA drift corrections. The final column presents the progression of the mean intensity within the ROI shown with blue and green circles throughout all repetitions. The signal intensity slightly increases when the drift correction is turned off, aligning with the simulation outcomes demonstrated in Supporting Information Figure S2.

scanners compared to the 1 kW amplifiers used in 9.4 and 7T Plus scanners. Separate evaluation of the RFPA drifting behavior at each site is recommended in light of these observations. The assessment of drift was conducted multiple times using different RF coils and loads (phantoms and subjects). Additionally, at one site, the measurement was repeated while the scanner was ramped down. Overall, it was observed that the aforementioned factors do not contribute to RFPA drift, or their contribution is minimal. Although all experiments in this study were conducted on UHF MR scanners, the observation of RFPA drift at lower fields with quadrature body coils is not unexpected.

This study investigated two k-space filling strategies: linear and centric. While linear ordering is the more common approach in Cartesian sampling, the centric reordering of k-space patterns is commonly preferred for sequences involving magnetization preparation or when the transient signal is of interest.[31–33] The steeper initial slope of the drift curve can result in a more noticeable change in global intensity in the image domain for centrically ordered acquisitions. This effect is evident through the higher CV observed in Figure 6 for the centrically ordered scan compared to the linearly ordered scan.

The predictive approach offers a lower implementation complexity. Unlike the run-time approach, it does not demand a heavy computational burden for real-time calculations, alteration of the reconstruction pipeline, and the integration of feedback mechanisms. However, this method necessitates the repetition of the entire protocol once to generate the RFPA drift curve, followed by offline calculations to determine the necessary corrections. This approach relies on the premise that the drift curve remains consistent when the same protocol is repeated, an assumption that has been verified as valid for the protocols

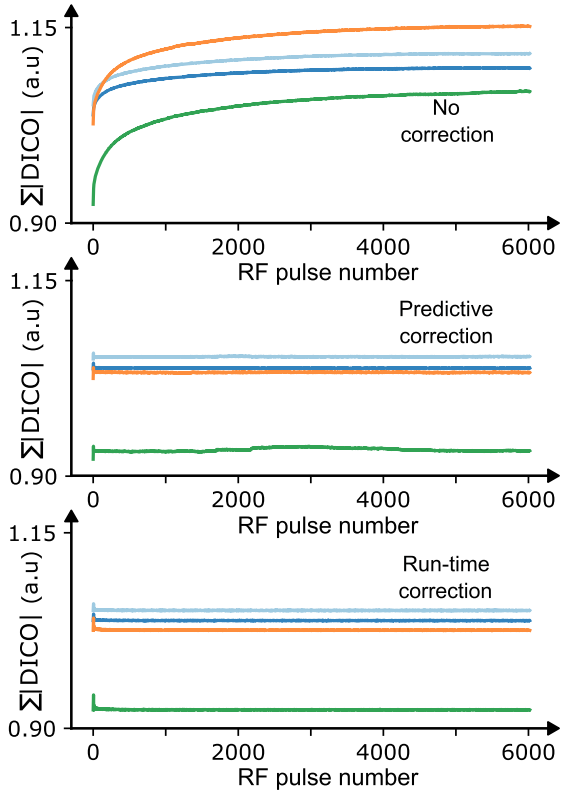

FIGURE 8 The evolution of radiofrequency (RF) power amplifier (RFPA) drift is depicted for no correction, predictive correction, and run-time correction. Ideally, all curves should remain entirely horizontal when there is no drift. Four representative transmit channels (1, 2, 13, and 16) are displayed for clarity. Each point on the plot corresponds to the integral of the magnitude of directional coupler records.

utilized in this study. Figure S4 exhibits a demonstration of the reproducibility of drift curves involving five measurements with a 10-s interval between each (TR = 3.5 ms, RF = 1 ms). In typical protocols, exporting raw-data and computing scale factors with predictive correction approach provides ample time for RFPA for complete relaxation. Nevertheless, in exceptionally high RF duty-cycle scenarios, it is recommended to contemplate extending this time period for a full relaxation and experimentally verify it for individual RFPAs.

When the transmit voltage remains constant, the correction table derived from one scan can be employed for the same scan in different sessions. However, it is important to note that in this study, slight instability was observed in certain RFPAs, which challenges the assumption of drift curve reproducibility. RFPAs exhibiting instability are those that deviate from the overall curve trend depicted in Figure 1. This instability is further evident in the predictive correction DICO plots displayed in Figure 8, where one RFPA, plotted in green, demonstrates this behavior. To address this concern, the run-time correction approach can be employed as a solution. The run-time approach eliminates the need for repeated scans as the correction factors are computed directly from the ongoing scan. This capability enables the cancellation of both drift and unexpected RFPA instability. However, it is important to account for the time lag between calculations and the application of correction factors. This lag can extend to several TRs when TR is very short. In the case of a TR of 3.2 ms, as utilized in this study for bSSFP sequence, the correction calculated for the nth pulse was applied to either the $(n + 2)$th or $(n + 3)$th pulse due to the time lag. The extent of lag is influenced by factors such as the RF length, the number of transmit channels, and the TR. In cases where the TR exceeded 15 ms and the RF length was 1 ms, it became feasible to reduce the delay to just one TR.

To achieve a fully established steady state, it is advisable to utilize a preparation scan of $5T_1$.[34] Because of the extended T_1 values of gray matter and white matter at 9.4T,[26] the transition to steady state requires approximately 10 s, during which RFPAs reach a stable output condition. In order to maintain the sensitivity to RFPA drift, only the initial seven repetitions were excluded for in vivo analysis. This determination was made based on the intensity curve of a representative voxel, plotted in the final column of Figure 7. This means that a total of 1136 RF pulses were employed as part of the preparation scan, with an average drift contribution of only 2.0% factoring into the CV calculation. Nevertheless, the variability in voxel intensity across the initial repetitions remains a combination of RFPA drift and the transient state of the bSSFP sequence. Disentangling the individual contributions from these two factors proves to be a challenging task. Simulation results indicated that the utilization of a low FA pulse could expedite the attainment of steady state. As demonstrated in Figure 3, the reduction in FA should not impact the maximum drift, provided the study remains within a low transmit voltage range. However, it has been illustrated in Figure S5 that for a constant RFPA drift, the MR signal exhibits decreased sensitivity to RFPA drift at lower FA values. To validate the proposed RFPA drift correction method, a custom-made spherical gel phantom with a T_1 relaxation time of 460 ms was employed. This choice enabled a notable reduction in the steady-state transition time.

4.1 | Potential benefit of RFPA drift correction

The sensitivity to RFPA drift varies based on the specific application. In certain cases, the impact of drift can be mitigated by running dummy scans, allowing the RFPA output to stabilize. However, this approach may not

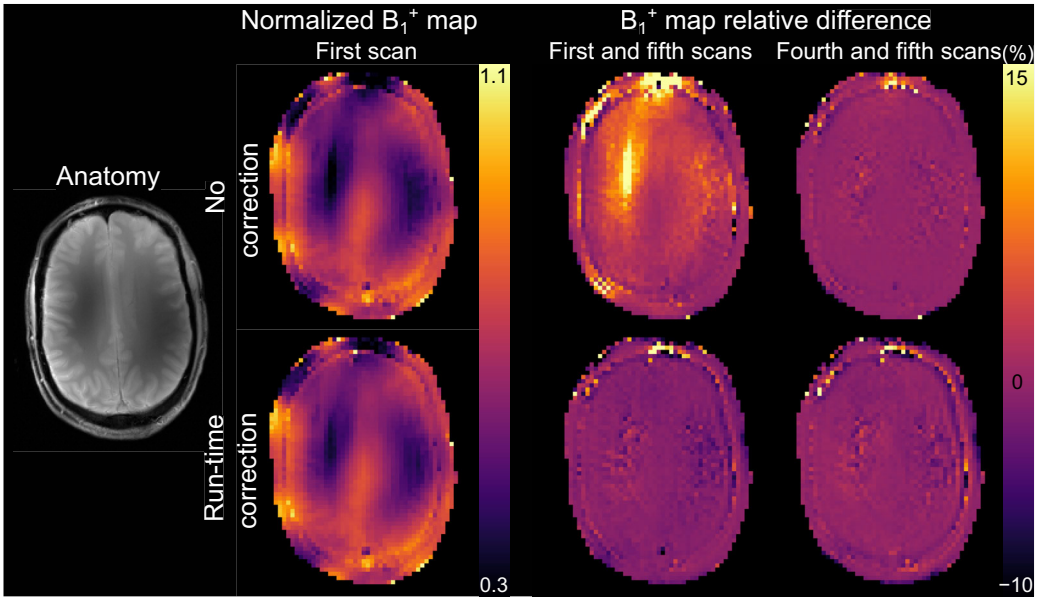

FIGURE 9 B_1^+ reproducibility is evaluated using two-dimensional presaturation TurboFLASH (satTFL) sequence while radiofrequency (RF) power amplifier (RFPA) drift correction turned off and on. Five sets of B_1^+ maps are generated from five consecutive measurements. Notably, the initial scan is more influenced by RFPA output drift compared to the later scans. Consequently, the relative difference between the B_1^+ maps calculated from the first and fifth scans is higher than the relative difference between the B_1^+ maps calculated from the fourth and fifth scans. With RFPA drift correction activated, the temporal drift at the outset becomes acceptably compensated, resulting in a reduction of the relative difference between the first and fifth B_1^+ maps. B_1^+ map displayed in the second column is normalized to its nominal value, set at 90°.

always be feasible. Particularly in UHF scenarios where B_1^+ inhomogeneity requires the use of parallel transmission, both B_1^+ mapping calibration scans and tailored RF pulses can be influenced by RFPA drift. This can raise disparity between simulations and actual measurements and needs to be considered. The unaccounted impact of RFPA drift could potentially compromise the accuracy and safety of SAR predictions. RFPAs with different magnitude/phase drifts can cause the SAR distribution to deviate from the expected distribution. Even if all RFPAs drift consistently with each other, the magnitude of the SAR will be overestimated or underestimated. While the scanner used in this study uses real-time SAR monitoring to measure power for all 16 channels, SAR lookahead is considered a redundancy to increase the fault tolerance of the SAR monitoring system, which is compromised by drifting RFPAs. In addition, underestimation of SAR by the prospective SAR supervision mechanism can cause nuisance if sequences are aborted by online SAR supervision if the two deviate due to RFPA drift.

Considering the long-standing aim of quantitative MRI to establish a common ground for quantitative tissue characteristics, which is ideally completely independent of any external instrumental factors and thus provides an objective reproducible measure, an understanding of the occurrence of RFPA drift and its correction is crucial. The results presented in this article indicate that RFPA drift could potentially affect the accuracy of any MR quantification method, which is sensitive to the RF excitation profile and flip angle, in particular in scenarios with high RF duty cycles and when using unregulated RF amplifiers. Candidates which could potentially benefit from an RFPA drift analysis and correction strategy include CEST and magnetization transfer experiments,[35] fingerprinting,[36] spin tomography in the time domain,[37] short-TR steady-state relaxometry,[38–42] or B_1^+ mapping sequences such as the investigated satTFL or Bloch–Siegert shift.[19]

The potential impact on quantitative MRI is corroborated by the performed B_1^+ mapping experiments using satTFL, which reveal that RFPA drift affects the reliability of the obtained B_1^+ values (cf. Figure 9). Errors in the estimation of B_1^+ can in turn considerably affect the quantification of tissue-specific parameters such as relaxation or diffusion metrics if the underlying MR acquisition is sensitive to B_1^+, which is, for example, the case for SSFP sequences. The simulation results presented in Figure S6 demonstrate for three SSFP-based T_1 mapping techniques—variable flip angle,[43] motion-insensitive rapid configuration relaxometry,[40] and triple echo steady state[42]—how errors in B_1^+ mapping can translate into a bias of T_1 estimation since those methods necessitate knowledge about B_1^+, which is typically obtained by an external B_1^+ mapping scan. The simulation reveals that a deviation of approximately 5% in B_1^+ leads to a corresponding deviation of about 10% in

T_1 for all investigated methods. As evident from Figure 9, RFPA drift can cause B_1^+ deviations exceeding 5% in large portions of the brain and as high as 15% in certain areas. Please note that motion-insensitive rapid configuration relaxometry and triple echo steady state allow the joint quantification of T_2 alongside T_1. In contrast to T_1, the T_2 estimation is largely independent of B_1^+ for these methods.[44] Generally, RFPA drift is expected to become the more apparent the shorter the scan times and should thus be considered especially in case of accelerated quantitative imaging with sparsely sampled data.

4.2 | Limitations

In the suggested RFPA drift correction approach, the reference is established using the integral of the magnitude of the initial RF pulse, with subsequent pulses scaled relative to this reference. This implies that the correction focuses solely on inter-pulse variations, striving to maintain a consistent RF integral. However, it is important to note that drift also occurs while the RF is actively transmitting, leading to modifications in the RF shape. For example, a rectangular RF pulse can be experienced as a right trapezoid, potentially affecting the excitation profile. This particular effect has not been explored or considered in the current work.

5 | CONCLUSIONS

The aim of this study was to investigate, comprehend, and correct for RFPA drift. The findings highlight that in typical imaging with a short TR and/or a long RF, RFPA can drift within a notable range. If not addressed, it can manifest as undesired signals, potentially affecting the reproducibility of data. The suggested approach involving predictive and run-time drift correction has shown encouraging results in mitigating drift. This involves monitoring DICO recordings to calculate drift and dynamically adjusting transmit voltages during the scanning. The suggested drift correction method also has the potential to enhance the accuracy and reproducibility of qMRI performed on an MR system equipped with unregulated amplifiers.

DATA AVAILABILITY STATEMENT

The code used for reading DICO recording from raw data and performing predictive correction is available at https://github.com/aghaeifar-publications/RFPA_drift. Binaries for run-time correction can be obtained through Siemens Healthineers customer-to-customer partnership program (C2P procedure).

ACKNOWLEDGEMENT

Open Access funding enabled and organized by Projekt DEAL.

ORCID

Ali Aghaeifar https://orcid.org/0000-0002-6964-0992
Dario Bosch https://orcid.org/0000-0002-6537-6370
Rahel Heule https://orcid.org/0000-0002-4589-6483
Sydney Williams https://orcid.org/0000-0001-9979-6245
Philipp Ehses https://orcid.org/0000-0002-5839-6525
Franck Mauconduit https://orcid.org/0000-0002-0128-061X
Klaus Scheffler https://orcid.org/0000-0001-6316-8773

REFERENCES

1. Thesen S, Kruger G, Muller E. Absolute correction of B0 fluctuations in echo-planar imaging. Paper presented at: Proceedings of the International Society of Magnetic Resonance in Medicine. Toronto, Canada; 2003:1025.
2. Benner T, Van der Kouwe AJW, Kirsch JE, Sorensen AG. Real-time RF pulse adjustment for B0 drift correction. *Magn Reson Med*. 2006;56:204-209.
3. Near J, Edden R, Evans CJ, Paquin R, Harris A, Jezzard P. Frequency and phase drift correction of magnetic resonance spectroscopy data by spectral registration in the time domain. *Magn Reson Med*. 2015;73:44-50.
4. Hui SCN, Mikkelsen M, Zöllner HJ, et al. Frequency drift in MR spectroscopy at 3T. *Neuroimage*. 2021;241:118430.
5. Lange T, Zaitsev M, Buechert M. Correction of frequency drifts induced by gradient heating in 1H spectra using interleaved reference spectroscopy. *J Magn Reson Imaging*. 2011;33:748-754.
6. Myer DP. Radiofrequency Power Amplifiers for NMR and MRI. In: Harris RK, Wasylishen RL, eds. *eMagRes*. John Wiley. https://doi.org/10.1002/9780470034590.emrstm1138
7. Gudino N, Heilman JA, Riffe MJ, Heid O, Vester M, Griswold MA. On-coil multiple channel transmit system based on class-D amplification and pre-amplification with current amplitude feedback. *Magn Reson Med*. 2013;70:276-289.
8. Hoult DI, Foreman D, Kolansky G, Kripiakevich D. Overcoming high-field RF problems with non-magnetic Cartesian feedback transceivers. *Magn Reson Mater Phys Biol Med*. 2008;21:15-29.
9. Zanchi MG, Stang P, Kerr A, Pauly JM, Scott GC. Frequency-offset Cartesian feedback for MRI power amplifier linearization. *IEEE Trans Med Imaging*. 2011;30:512-522.
10. Lebsack ET, Wright SM. Iterative RF pulse refinement for magnetic resonance imaging. *IEEE Trans Biomed Eng*. 2002;49:41-48.
11. Stang PP, Pauly JM, Scott GC. A versatile in-line sensor for power monitoring and calibration of transmit arrays. Paper presented at: Proceedings of the 17th Annual Meeting of ISMRM, vol. 3024. 2009; Honolulu, Hawaii. 3024
12. Stang PP, Kerr AB, Grissom W, Pauly JM, Scott GC. Vector iterative pre-distortion: an auto-calibration method for transmit arrays. Paper presented at: Proceedings of the 17th Annual Meeting of ISMRM. Hawaii; 2009:395.

13. Çavuşoğlu M, Dietrich BE, Brunner DO, Weiger M, Pruessmann KP. Correction of parallel transmission using concurrent RF and gradient field monitoring. *Magn Reson Mater Phys Biol Med*. 2017;30:473-488.
14. Grissom WA, Kerr AB, Stang P, Scott GC, Pauly JM. Minimum envelope roughness pulse design for reduced amplifier distortion in parallel excitation. *Magn Reson Med*. 2010;64: 1432-1439.
15. Ibrahim TS, Lee R, Baertlein BA, Kangarlu A, Robitaille P-ML. Application of finite difference time domain method for the design of birdcage RF head coils using multi-port excitations. *Magn Reson Imaging*. 2000;18:733-742.
16. Feng K, Hollingsworth N, McDougall MP, Wright SM. A 64-channel transmitter for investigating parallel transmit MRI. *IEEE Trans Biomed Eng*. 2012;59:2152-2160.
17. Voelker MN, Kraff O, Goerke S, et al. The traveling heads 2.0: Multicenter reproducibility of quantitative imaging methods at 7 tesla. *Neuroimage*. 2021;232:117910.
18. Sherif S, Aghaeifar A, Seif M, et al. Repeatability of ultra-high-resolution multi-parametric mapping across five 7T sites. Paper presented at: Joint Annual Meeting ISMRM-ESMRMB. London, United Kingdom; 2022. Abstract 2788
19. Sacolick LI, Wiesinger F, Hancu I, Vogel MW. B1 mapping by Bloch-Siegert shift. *Magn Reson Med*. 2010;63:1315-1322.
20. Shajan G, Kozlov M, Hoffmann J, Turner R, Scheffler K, Pohmann R. A 16-channel dual-row transmit array in combination with a 31-element receive array for human brain imaging at 9.4 T. *Magn Reson Med*. 2014;71:870-879.
21. Jaeschke SHF, Robson MD, Hess AT. Scattering matrix imaging pulse design for real-time respiration and cardiac motion monitoring. *Magn Reson Med*. 2019;82:2169-2177.
22. Williams SN, Allwood-Spiers S, McElhinney P, et al. A nested eight-channel transmit array with open-face concept for human brain imaging at 7 tesla. *Front Phys*. 2021;9:9.
23. Hess AT, Tunnicliffe E, Rodgers CT, Robson MD. Diaphragm position can be accurately estimated from the scattering of a parallel transmit RF coil at 7 T. *Magn Reson Med*. 2018;79:2164-2169.
24. Chung S, Kim D, Breton E, Axel L. Rapid B1+ mapping using a preconditioning RF pulse with TurboFLASH readout. *Magn Reson Med*. 2010;64:439-446.
25. Bieri O, Markl M, Scheffler K. Analysis and compensation of eddy currents in balanced SSFP. *Magn Reson Med*. 2005;54:129-137.
26. Zhu J, Klarhöfer M, Santini F, Scheffler K, Bieri O. Relaxation measurements in brain tissue at field strengths between 0.35 T and 9.4 T. Paper presented at: Joint Annual Meeting ISMRM-ESMRMB. Milan, Italy; 2014. Abstract 3208
27. Graesslin I, Krueger S, Vernickel P, Achtzehn J, Nehrke K, Weiss S. Detection of RF unsafe devices using a parallel transmission MR system. *Magn Reson Med*. 2013;70:1440-1449.
28. Graesslin I, Vernickel P, Börnert P, et al. Comprehensive RF safety concept for parallel transmission MR. *Magn Reson Med*. 2015;74:589-598.
29. Landes V, Nayak KS. Iterative correction of RF envelope distortion with GRATER-measured waveforms. *Magn Reson Med*. 2020;83:188-194.
30. Brunner D, Dietrich B, Çavuşoğlu M, et al. Concurrent recording of RF pulses and gradient fields–comprehensive field monitoring for MRI. *NMR Biomed*. 2016;29:1162-1172.
31. Bosch D, Bause J, Geldschläger O, Scheffler K. Optimized ultrahigh field parallel transmission workflow using rapid presaturated TurboFLASH transmit field mapping with a three-dimensional centric single-shot readout. *Magn Reson Med*. 2023;89:322-330.
32. Zaiss M, Ehses P, Scheffler K. Snapshot-CEST: optimizing spiral-centric-reordered gradient echo acquisition for fast and robust 3D CEST MRI at 9.4 T. *NMR Biomed*. 2018;31:e3879.
33. Worters P, Hargreaves BA. Balanced SSFP transient imaging using variable flip angles for a predefined signal profile. *Magn Reson Med*. 2010;64:1404-1412.
34. Bieri O, Scheffler K. Fundamentals of balanced steady state free precession MRI. *J Magn Reson Imaging*. 2013;38:2-11.
35. Van Zijl PCM, Lam WW, Xu J, Knutsson L, Stanisz GJ. Magnetization transfer contrast and chemical exchange saturation transfer MRI. Features and analysis of the field-dependent saturation spectrum. *Neuroimage*. 2018;168:222-241. Neuroimaging with Ultra-high Field MRI: Present and Future.
36. Ma D, Coppo S, Chen Y, et al. Slice profile and B1 corrections in 2D magnetic resonance fingerprinting. *Magn Reson Med*. 2017;78:1781-1789.
37. Sbrizzi A, Heide O, Cloos M, et al. Fast quantitative MRI as a nonlinear tomography problem. *Magn Reson Imaging*. 2018;46:56-63.
38. Deoni S. High-resolution T1 mapping of the brain at 3T with driven equilibrium single pulse observation of T1 with high-speed incorporation of RF field inhomogeneities (DESPOT1-HIFI). *J Magn Reson Imaging*. 2007;26:1106-1111.
39. Weiskopf N, Suckling J, Williams G, et al. Quantitative multi-parameter mapping of R1, PD*, MT, and R2* at 3T: a multi-center validation. *Front Neurosci*. 2013;7:95.
40. Nguyen D, Bieri O. Motion-insensitive rapid configuration relaxometry. *Magn Reson Med*. 2017;78:518-526.
41. Shcherbakova Y, Van den Berg CAT, Moonen C, Bartels LW. PLANET: an ellipse fitting approach for simultaneous T1 and T2 mapping using phase-cycled balanced steady-state free precession. *Magn Reson Med*. 2018;79:711-722.
42. Heule R, Ganter C, Bieri O. Triple echo steady-state (TESS) relaxometry. *Magn Reson Med*. 2014;71:230-237.
43. Heule R, Ganter C, Bieri O. Variable flip angle T1 mapping in the human brain with reduced t2 sensitivity using fast radiofrequency-spoiled gradient echo imaging. *Magn Reson Med*. 2016;75:1413-1422.
44. Ganter C. Approximate B1+ scaling of the SSFP steady state. *Magn Reson Med*. 2023;89:2264-2269.

SUPPORTING INFORMATION

Additional supporting information may be found in the online version of the article at the publisher's website.

Figure S1. A comparison between no RFPA drift correction, predictive RFPA drift correction, and run-time RFPA drift correction in a phantom study with centric reordered k-space sampling pattern. The initial repetition is excluded from the analysis to mitigate the impact of the transient state. The utilization of RFPA correction leads to more uniform CV values similar to the results shown in Figure 5.

Figure S2. The signal evolution simulation is conducted for a bSSFP sequence by applying a train of preparation pulses using two different T_1 values: 460 ms and 2000 ms. The dashed lines of the same color represent the simulation results in the presence of drift. The plotted curves reveal several insights. Firstly, for FA of 15°, the steady-state signal with a T_1 value of 460 ms achieves a higher level. Moreover, the signal exhibits a gradual increase and takes more time to reach a steady state. On the other hand, for $T_1 = 2000$ ms, the discrepancy between the ideal and drifted simulations is significantly smaller compared to the case with $T_1 = 460$ ms.

Figure S3. A comparison of CV is presented for the second subject who participated in the study. The analysis includes the scenarios of no RFPA drift correction and the two proposed approaches for drift correction. Similar to the results obtained from subject 1, the first seven repetitions are excluded from the analysis to minimize the contribution of the transient state. However, due to the extended T_1 of GM and WM at 9.4T, the computed CV reflects a combined impact of the transient state and RFPA drift. The last column of the figure illustrates the evolution of voxel intensity, represented by the blue cross in the first column, across all repetitions.

Figure S4. Demonstrating the reproducibility in RFPA drifting magnitude. A single slice is measured using the bSSFP sequence five times (TR=3.5ms, RF=1ms), with a 10-second delay between measurements to enable relaxation of the RFPA. The necessary delay for RFPA relaxation is determined experimentally. Drifting in six exemplary Tx channels is depicted for simplicity. The predictive correction approach is based on the consistency of the drifting curve between calibration and correction scans. It is important to note that potential distortion may occur due to RFPA malfunctions, which are not reproducible.

Figure S5. The obtained MR signal originates from the transverse component of magnetization, and its magnitude is correlated to the flip angle (FA) through the sine function. The figure illustrates the discrepancy in the magnitude of the transverse component between the ideal excitation and the drifted excitation for various FA values, considering possible drift effects.

Figure S6. T_1 bias (y axis) resulting from a B_1^+ quantification error (x axis) for variable flip angle (VFA), motion-insensitive rapid configuration relaxometry (MIRACLE), and triple echo steady state (TESS). Simulation parameters: TR = 5 ms, T_1 / T_2 = 1425 ms / 29 ms corresponding to WM at 9.4T reported in literature, actual (true) $B_1^+ = 1.0$, flip angles: 3°/15° (VFA), 10° (MIRACLE/TESS), RF spoiling increment: 50° (VFA). B_1^+ and T_1 errors were defined as: $\Delta B_1^+ = ((B_{1,est}^+ - B_{1,act}^+)/B_{1,act}^+) \cdot 100$, $\Delta T_1 = ((T_{1,est} - T_{1,act})/T_{1,act}) \cdot 100$ with estimated (est) and actual/true (act) values. The B_1^+ error is referring to potential inaccuracies in the employed external B_1^+ mapping method. MIRACLE and TESS exhibit the same B_1^+ sensitivity since relaxometry is based on the same signal equations, but different acquisition schemes.

How to cite this article: Aghaeifar A, Bosch D, Heule R, et al. Intra-scan RF power amplifier drift correction. *Magn Reson Med*. 2024;1-15. doi: 10.1002/mrm.30078